

www.acsami.org Research Article

# Potential Solid-State Electrolytes with Good Balance between Ionic Conductivity and Electrochemical Stability: $\text{Li}_{5-x}M_{1-x}M_x'O_4$ (M = Al and Ga and M' = Si and Ge)

Bingkai Zhang,\* Jiajie Zhong, Feng Pan,\* and Zhan Lin\*



Cite This: ACS Appl. Mater. Interfaces 2021, 13, 61296-61304



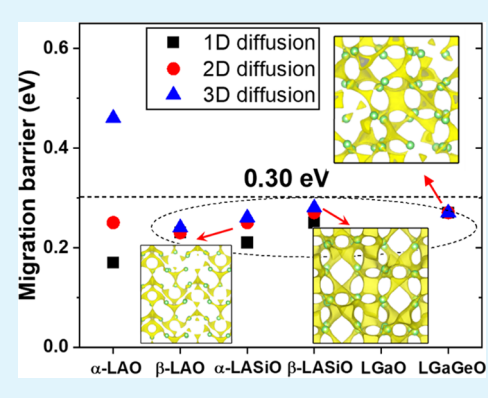
**ACCESS** 

Metrics & More

Article Recommendations

s Supporting Information

ABSTRACT: Exploring new solid-state electrolyte (SSE) materials with good electrochemical stability and high Li-ion conductivity for all-solid-state Li-ion batteries is vital for the development of technologies. Herein, we employ two lithium aluminates,  $\alpha$ - and  $\beta$ -Li<sub>5</sub>AlO<sub>4</sub> ( $\alpha$ - and  $\beta$ -LAO), as the model framework, which have an orthorhombic crystal structure and isolated AlO<sub>4</sub> tetrahedron units connected in lithium atoms, exhibiting large band gaps, low migration barriers (0.30–0.40 eV), fast Li-ion conductivity (LIC, in a magnitude of  $10^{-4}$  S/cm), and a good electrochemical stability window (ESW, [0.01–3.20 V] vs Li<sup>+</sup>/Li). We tabulate the expected decomposition products at the interface, while considering cathodes in combination with the LAO electrolyte to discuss their compatibility. We also examine the electrochemical stability, H<sub>2</sub>O/CO<sub>2</sub> stability, and Li-ion mobility of Li<sub>4.6</sub>Al<sub>0.6</sub>Si<sub>0.4</sub>O<sub>4</sub> (LASO), Li<sub>5</sub>GaO<sub>4</sub> (LGaO), and Li<sub>4.6</sub>Ga<sub>0.6</sub>Ge<sub>0.4</sub>O<sub>4</sub> (LGaGeO) compounds. In general, there is usually a trade-off between the LIC and the ESW;



however, LAO features a good balance between an outstanding LIC and a wide ESW, making the compound a promising candidate for next-generation SSE materials.

KEYWORDS: Li<sub>S</sub>AlO<sub>4</sub>, solid-state electrolyte, ionic conductivity, stability, first-principles calculations, all-solid-state lithium-ion battery

### 1. INTRODUCTION

New solid-state electrolyte (SSE) materials that can fast transport Li-ions from one electrode to the other are required to increase energy density and decrease safety concerns in allsolid-state lithium-ion batteries (ASSLBs). 1,2 Such SSE materials can thus help to alleviate technological challenges associated with the adoption of electric vehicles and accelerate the transition to a low-carbon economy. The most commonly used SSE materials, such as sulfide-based lithium superionic conductors (LISICON),<sup>3,4</sup> oxide-based NASICON-like conductors (sodium superionic conductors),<sup>5</sup> garnet,<sup>6,7</sup> and perovskites, 8,9 have Li-ion conductivities approaching those of liquid electrolytes. However, current SSE materials are not stable against lithium-ion battery electrodes, especially for cathode materials. 10,11 Moreover, we could count on one hand the number of oxide SSE materials. Therefore, there is an urgent need for new SSE materials with high Li-ion conductivity and electrochemical (chemical) stability. 12

In our present work, we investigate the less-studied lithium aluminate,  $\text{Li}_5\text{AlO}_4$  (LAO), which is previously used as a coating material on  $\text{LiNi}_x\text{Co}_y\text{Mn}_z\text{O}_2$  cathodes,  $^{13,14}$  a gate dielectric,  $^{15}$  and a high-temperature  $\text{CO}_2$ -capturing material.  $^{16}$  This crystalline LAO has two polymorphs that are  $\alpha$ - and  $\beta$ -crystallized LAO phases, and both phases crystallize in an orthorhombic structure, characterized by the *Pbca* space group with a=9.087, b=8.947, and c=9.120 Å and the *Pmmn* space

group with a = 6.420, b = 6.302, and c = 4.620 Å, respectively. Both structures are ordered derivatives of the antifluorite (Li<sub>2</sub>O) structure and the cation atoms' (Li and Al) ordered arrangement causes an orthorhombic distortion from cubic symmetry. LAO can potentially permit a high ionic conductivity with a three-dimensional (3D) percolating diffusion network. Therefore, it is anticipated that bulk LAO can have high ion conductivity. Nevertheless, to date, only two early experiments <sup>17,18</sup> have been reported on the utilization of this material as a SSE except a computation research using a high-throughput method, <sup>19</sup> but the analysis of structure—property relationships in LAO and Si/Ge-substituted compositions for SSE has been unknown.

Herein, we apply first-principles density functional theory (DFT) to understand their stability and ion conductivity. We calculate the formation energies of several defects in the range of 0-4.5 V versus Li/Li<sup>+</sup>. We evaluate the electrochemical stability window and  $H_2O/CO_2$  stability of LAO, LASO,

Received: October 20, 2021 Accepted: December 2, 2021 Published: December 14, 2021





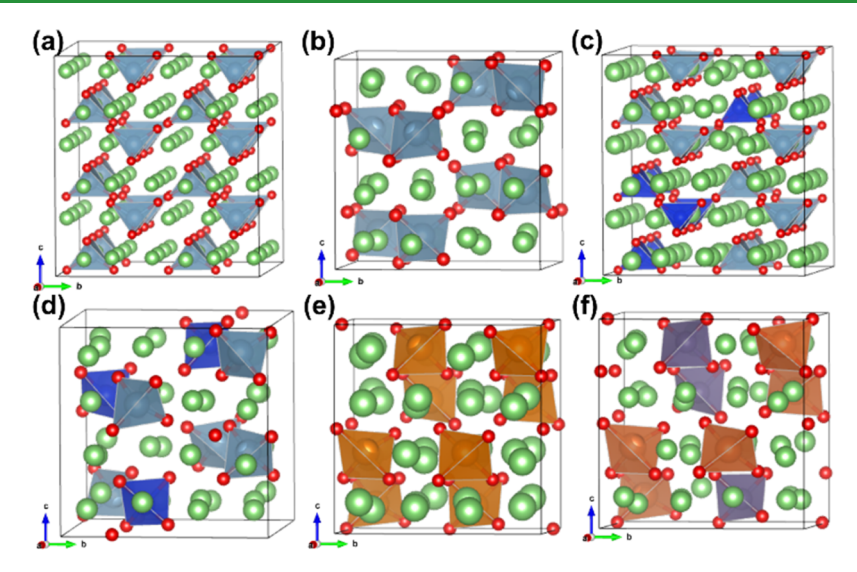


Figure 1. (a–f) Side view of α-LAO with the *Pmmn* space group,  $\beta$ -LAO with the *Pbca* space group, α-Li<sub>4.6</sub>Al<sub>0.6</sub>Si<sub>0.4</sub>O<sub>4</sub> (α-LASiO),  $\beta$ -Li<sub>4.6</sub>Al<sub>0.6</sub>Si<sub>0.4</sub>O<sub>4</sub> ( $\beta$ -LASiO), Li<sub>5</sub>GaO<sub>4</sub> (LGaO) with the *Pbca* space group, and the Li<sub>4.6</sub>Ga<sub>0.6</sub>Ge<sub>0.4</sub>O<sub>4</sub> (LGaGO) crystal structure, respectively. The green and red spheres, dusty and dark blue tetrahedrons, orange and gray red tetrahedrons represent the Li and O atoms, AlO<sub>4</sub> and SiO<sub>4</sub> units, GaO<sub>4</sub>, and GeO<sub>4</sub> units, respectively.

LGaO, and LGaGeO compounds and tabulate the expected decomposition products at the cathode/LAO and cathode/LGaO interfaces. We employed the bond valence site energy (BASE) method and DFT-based climbing image nudged elastic band (Cl-NEB) simulations to evaluate the Li-ion mobility and found that the ion conductivity of LAO and LGaO is on a par with known SSE materials, which is critical for the operation of ASSLBs .

# 2. COMPUTATIONAL DETAILS

All calculations in this work were performed with a general gradient approximation applying the Perdew–Burke–Ernzerhof functional, in the program of the Vienna Ab initio Simulation Package (VASP). Valence electron configurations are expanded with the projector augmented wave basis set. Monkhorst–Pack k-point meshes  $(2 \times 2 \times 2)$  and  $(3 \times 3 \times 3)$  were used to sample the Brillouin zones for a  $p(2 \times 2 \times 2)$   $\alpha$ -LAO supercell and  $\beta$ -LAO unit cell, respectively. The cutoff energy for plane-wave expansion was set to 500 eV. Residual force less than 0.01 eV/Å and total energy less than  $10^{-5}$  eV were utilized for all the calculations.

The substitution of each  $M^{3+}$  by  $M'^{3+}$  needs to delete a Li atom for charge compensation. According to the calculated configuration energy, Si/Ge-dopants in LAO/LGaO tend to have a dispersed distribution rather than agglomeration, and the Li vacancies are nearby the  $M'^{3+}$  cations. To evaluate the interaction between one Li-ion and one  $XO_4$  unit (X = Al, Si, Ga, and Ge), one Li and one  $XO_4$  are set in a  $20 \times 20 \times 20$  Å lattice. To calculate the bond dissociation energy of X–O, one  $XO_4$  and one  $XO_3$  are set in a  $20 \times 20 \times 20$  Å lattice, respectively. During the relaxation, the atomic positions of  $XO_4$  are fixed but Li is allowed to relax. The X–O bond lengths were obtained from  $Li_5AlO_4$  (COD-1523841),  $Li_4SiO_4$  (COD-4124128),  $Li_5GaO_4$  (COD-1528895), and  $Li_4GeO_4$  (COD-9008154). COD represents the Crystallography Open Database.

The formation energy  $E_{\rm f}$  of a defect is defined as the following equation

$$E_{\rm f} = E_{\rm tot}({\rm defect}, q) - E_{\rm tot}({\rm bulk}) - n_i \mu_i + q(E_{\rm VBM} + \mu_{\rm e})$$
(1)

Herein,  $E_{tot}(defect, q)$  is the total energy of the defect system with charge q,  $E_{tot}(bulk)$  is the total energy of a bulk supercell of the same size as the defected one, and  $n_i\mu_i$  is the reference energy of  $n_i$  added atoms of an element at chemical potential  $\mu_i$ . Applied voltage V can be directly converted to lithium chemical potential  $\mu_{\rm Li}$  using the equation  $\mu_{\rm Li} = {\mu_{\rm Li}}^0$  – eV, where  $\mu_{\rm Li}^{0}$  is the lithium chemical potential in the Li metal and e is the elementary charge. The term in the parenthesis accounts for the chemical potential of the electron involved in charging the defect.  $E_{VBM}$  is the valence band maximum for the bulk phase and  $\mu_e$  is the electron chemical potential and is treated as the Fermi level  $(E_f)$ . A negative  $E_f$  value suggests that the formation of a defect is exothermic and favorable. To search for the possible Li-ion migration pathways and the corresponding migration barriers, the BASE calculations using the softBV software tool<sup>25,26</sup> and the Cl-NEB method<sup>27,28</sup> were carried out. A  $\gamma$ -only k-point in the  $p(2 \times 2 \times 2)$   $\alpha$ -LAO supercell and  $\beta$ -LAO unit cell is considered. In the ab initio molecular dynamics (AIMD) simulations, an NVT ensemble was simulated using a time step of 2 fs with a period of 10 ps and a Nosé-Hoover thermostat. The Li-ion diffusion coefficient is calculated using the following formula.

$$D_{\rm Li} = \frac{1}{2} \nu (\Delta x)^2 \, e^{[-E_{\rm A}/k_{\rm B}T]} \tag{2}$$

where  $\Delta x$  is the hop distance,  $\nu$  is the lattice vibrational frequency with a typical value of  $10^{13}$  Hz, T is the temperature,  $k_{\rm B}$  is the Boltzmann constant, and  $E_{\rm A}$  is the migration barrier. The Li-ion conductivity ( $\sigma_{\rm Li}$ ) is estimated from the Nernst–Einstein relation

$$\sigma_{\rm Li} = n_{\rm Li} D_{\rm Li} \left( \frac{q^2}{k_{\rm B} T} \right) \tag{3}$$

where  $n_{\rm Li}$  is the concentration of Li-ions, q is the electrical charge of the diffusion carrier (Li),  $D_{\rm Li}$  is calculated from eq 2, and T is the temperature.

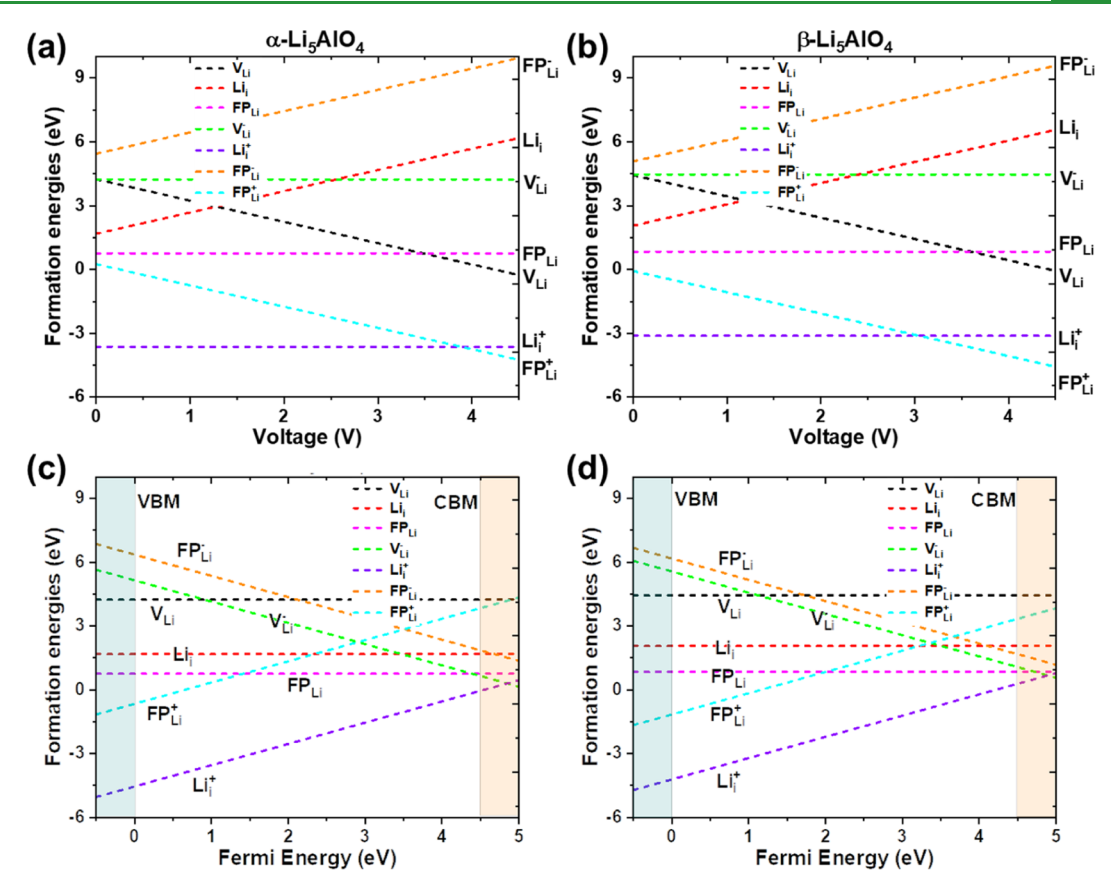


**Figure 2.** Formation energies,  $E_0$  for point defects as a function of applied voltage when the Fermi level at the valence-band maximum (a,b) and the Fermi level when the electrode potential is 0 V (c,d) in *α*- and *β*-LAO, respectively.

The electrochemical stability window of SSE materials means that they are stable at the applied voltage V. The electrochemical stability window (exactly on the grand potential convex hull) is determined by grand canonical linear programming (GCLP). The grand potential convex hull at a given voltage is formed by the grand potentials of a set of phases and their linear combinations that minimize the grand potential at each composition. More information about the calculations of electrochemical stability is detailed in previous studies. To study the  $H_2O$  and  $CO_2$  stability of LAO, we calculate  $\Delta E_{\text{mixing energy}}$  of the reactions:  $x\text{LAO} + (1-x)H_2O \rightarrow C_{\text{equilibrium}}$  and  $x\text{LAO} + (1-x)CO_2 \rightarrow C_{\text{equilibrium}}$ , which is defined as

$$\Delta E_{\text{mixing-energy}} = [E(C_{\text{equilibrium}}) - (1 - x)E(CO_2) - xE(LAO)]/n_{\text{atoms}}$$
(4)

$$\Delta E_{\text{mixing-energy}} = [E(C_{\text{equilibrium}}) - (1 - x)E(H_2O) - xE(LAO)]/n_{\text{atoms}}$$
(5)

where  $n_{\text{atoms}}$  represents the total number of atoms involved in the mixing reaction.

# 3. RESULTS AND DISCUSSION

**3.1. Structure Modeling and Defect Chemistry.** All crystal structures used in this work including  $\alpha$ - and  $\beta$ -LAO,  $\alpha$ -LASiO,  $\beta$ -LASiO, LgaO, and LGaGeO are shown in Figure 1a–f, respectively. Both structures of  $\alpha$ - and  $\beta$ -LAO (see Figure S1a,b in the Supporting Information) have an

orthorhombic symmetry and are composed of isolated AlO<sub>4</sub> units and corner-sharing or edge-sharing LiO<sub>4</sub> units, which are linked together to form 3D diffusion channels. There are two and eight formula units in  $\alpha$ - and  $\beta$ -LAO unit cells, respectively. Table S1 in the Supporting Information lists the calculation results of lattice parameters for both structures. The total density of states (TDOS) (see Figure S1c) shows that the bandgap of  $\alpha$ - and  $\beta$ -LAO is 4.87 and 4.98 eV, respectively, indicating that LAO materials are good electron insulators and thus block the electron leakage and protect against electron corrosion. In addition, the *Pbca*-phase LGaO also exhibits a large bandgap of 3.70 eV (see Figure S1c).

Calculations on intrinsic defects in the LAO system are performed on the optimized structure. Following eq 1, we obtain the formation energies of several defects (V<sub>Li</sub>: Li vacancy, Li: Li interstitial, FP1: Li Frenkel pair, and the + and - superscripts represent a hole and an electron, respectively). For V<sub>Li</sub> and Li defects, the most stable configurations are considered in the plots of Figure 2, which show the defect formation energies with applied voltage. It is found that the V<sub>Li</sub> and Li, are unfavorably thermodynamic at 0 K in the voltage range of 0-4.0 V because of the valence state of Al. The formation energy of  $V_{Li}$  (4.24 eV in  $\alpha$ -LAO and 4.44 eV in  $\beta$ -LAO) is much higher than that of Li<sub>i</sub> (1.68 eV in  $\alpha$ -LAO and 2.06 eV in  $\beta$ -LAO) at 0 V (corresponding to the lithium metal anode). This translates into a concentration over 43 and 30 orders of magnitude higher than that of  $V_{Li}$  according to c = N $\exp(-E_f/kT)$  in  $\alpha$ -LAO and  $\beta$ -LAO, respectively, indicating that Li, is the dominant conduction carrier under anodic conditions. However, the formation energy of  $V_{Li}$  (-0.26 eV in

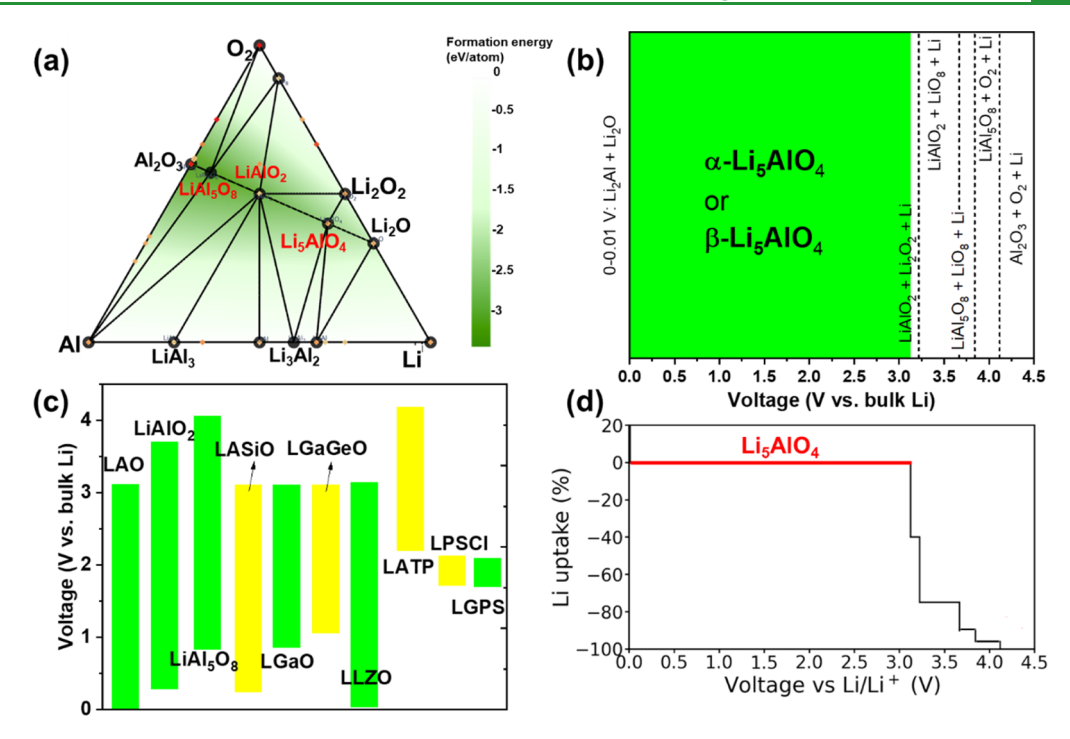


Figure 3. (a) Li–Al–O<sub>2</sub> phase diagram at 0 K computed from the LAO DFT data combined with Materials Project data, respectively. The green regions in the phase diagram become darker as the formation energy values are more negative. (b) Voltage profile and phase equilibria of LAO upon the lithiation and delithiation. The green-shaded region is determined after consideration of the energy of the Li insertion/extraction only without any mixing reaction from electrodes. (c) Electrochemical stability windows (green bar) for Li<sub>5</sub>AlO<sub>4</sub>, LiAlO<sub>2</sub>, LiAl<sub>5</sub>O<sub>8</sub>, Li<sub>7</sub>La<sub>3</sub>Zr<sub>2</sub>O<sub>12</sub> (LLZO), Li<sub>13</sub>Al<sub>03</sub>Ti<sub>1.7</sub>(PO<sub>4</sub>)<sub>3</sub> (LATP), Li<sub>6</sub>PS<sub>5</sub>Cl (LiPSCl), and Li<sub>10</sub>GeP<sub>2</sub>S<sub>12</sub> (LGPS) (for comparison) are shown. The yellow region reflects the possible extension of the voltage window. (d) Li uptake vs voltage for the LAO system.

 $\alpha$ -LAO and -0.06 eV in  $\beta$ -LAO) is much lower than that of Li<sub>i</sub> (6.18 eV in  $\alpha$ -LAO and 6.56 eV in  $\beta$ -LAO) at 4.5 V (corresponding to the high-voltage cathode environment), indicating that under cathodic conditions, the concentration of V<sub>Li</sub> is larger than that of Li<sub>i</sub>. It can be also seen that the formation energies of FP<sub>Li</sub><sup>+</sup> and Li<sub>i</sub><sup>+</sup> are lower than those of FP<sub>Li</sub> and Li<sub>i</sub>, implying that interstitial Li would spontaneously ionize in LAO. This can be rationalized by the fact that during Li-ion battery operation, FPLi and Li will change the charge state of Al and O and thus lead to phase transformations of LAO. For synthetic crystals by experiment, LAO can hardly exhibit off-stoichiometric composition as the valence state of Al ions is hard to change. It is known, however, the concentrations of intrinsic defects can be introduced into the system by cation-doping, such as the partial substitution of M<sup>3+</sup> by  $M'^{4+}$  or  $Zn^{2+}$ .

**3.2.** Electrochemical Stability, Interfacial Stability, and H<sub>2</sub>O/CO<sub>2</sub> Stability. Next, we employ the LAO as a model framework to evaluate the phase stability and electrochemical stability at 0 K computed from DFT data combined with python materials genomics code. The Li-Al-O ternary 0 K phase diagrams of Figure 3a depict the phase equilibria of LAO at different Li or O chemical potentials. The higher Li or O chemical potential, the farther away from the Li metal or the O<sub>2</sub> endpoint in the phase diagram, and vice versa. Within the Li<sub>2</sub>O-Al<sub>2</sub>O<sub>3</sub> combination, from the Al-rich side to Li-rich side, there are three Li<sub>x</sub>Al<sub>y</sub>O<sub>z</sub> compounds: Li<sub>5</sub>AlO<sub>4</sub>, LiAlO<sub>2</sub>, and LiAl<sub>5</sub>O<sub>8</sub>. Based on the formation energy (in different shades of color), the more the negative formation energy, the more stable the compound is likely to be. Figure 3b,d shows the electrochemical phase equilibria and Li uptake versus voltage for the LAO system, respectively. LAO exhibits

an anodic (cathodic) limit of 0.01 V (3.20 V) versus Li/Li<sup>+</sup>. It is noticeable that LAO will be unstable at high voltage and the phase decomposition, Li<sub>5</sub>AlO<sub>4</sub> → LiAlO<sub>2</sub> + Li<sub>2</sub>O<sub>2</sub> + Li, begins to occur at 3.2 V. Figure 3c shows that the intrinsic stability windows of these three Li Al O compounds are relatively wide. The detailed voltage profile and phase equilibria of LASiO, LGaO, and LGaGeO upon lithiation and delithiation are shown in Figures S2-S4 in the Supporting Information, respectively. The comparison of the electrochemical stability window between Li<sub>x</sub>Al<sub>y</sub>O<sub>z</sub> compounds and typical SSE materials suggests that LAO is on a par with LLZO. As compared with LATP, LPSCl, and LGPS materials, the electrochemical stability of LAO is much more superior. The comparison of the electrochemical stability window between the Li<sub>x</sub>Al<sub>y</sub>O<sub>z</sub> compounds and typical SSE materials suggests that LAO is on a par with LLZO. It is worth mentioning that LAO has the lowest reduction voltage among all listed materials, indicating that although LAO has less phase stability compared to other Li, Al, O, compounds, it still holds promise for use in Li-metal anodes. As compared with LATP, LPSCl, and LGPS materials, the electrochemical stability of LAO is much more superior.

To understand the interfacial electrochemical reaction between the LAO and conventional cathodes, we also apply the above method and consider all possible electrochemical reactions: xCathode + (1-x)LAO +  $ne^- \rightarrow C_{\text{equilibrium}}$ , where  $C_{\text{equilibrium}}$  is the low-energy phase equilibrium determined from the phase diagram and x is the mixing parameter varying from 0 and 1. The chemical reaction of LAO with cathode (xCathode + (1-x)LAO  $\rightarrow C_{\text{equilibrium}}$ ) and pure redox decomposition reaction of LAO (LAO +  $ne^- \rightarrow C_{\text{equilibrium}}$ ) are also shown in the second and third columns in Table 1,

Table 1. Predicted Chemical Reaction between the Cathode and LAO (xCathode + (1-x)LAO  $\rightarrow C_{\text{equilibrium}}$ ), LAO Redox Decomposition at Cathode Potential (LAO +  $ne^- \rightarrow C_{\text{equilibrium}}$ ), and the Electrochemical Reaction Products for the Cathode/LAO (xCathode + (1-x)LAO +  $ne^- \rightarrow C_{\text{equilibrium}}$ ) Mixing Reaction at Cathode Potential

cathode/LAO	chemical reaction	LAO redox decomposition at cathode potential <sup>a</sup>	electrochemical reaction with mixing at cathode potential <sup>a</sup>
LiCoO <sub>2</sub> /Li <sub>5</sub> AlO <sub>4</sub>	none	Li <sub>2</sub> O, Al <sub>2</sub> O <sub>3</sub>	none
LiNiO <sub>2</sub> /Li <sub>5</sub> AlO <sub>4</sub>	none	Li <sub>2</sub> O, Al <sub>2</sub> O <sub>3</sub>	Al <sub>2</sub> NiO <sub>4</sub> , Li <sub>2</sub> O
LiMnO <sub>2</sub> /Li <sub>5</sub> AlO <sub>4</sub>	none	LiAl <sub>5</sub> O <sub>8</sub> , Li <sub>2</sub> O	$LiAl_5O_8$ , $Li_4Mn_5O_{12}$
NCM532 <sup>b</sup> /Li <sub>5</sub> AlO <sub>4</sub>	none	Li <sub>2</sub> O, Al <sub>2</sub> O <sub>3</sub>	Li <sub>2</sub> O, MnNiO <sub>3</sub> , CoO <sub>2</sub> , Al <sub>2</sub> NiO <sub>4</sub>
NCM811 <sup>b</sup> /Li <sub>5</sub> AlO <sub>4</sub>	none	Li <sub>2</sub> O, Al <sub>2</sub> O <sub>3</sub>	Li <sub>2</sub> O, MnNiO <sub>3</sub> , CoO <sub>2</sub> , Al <sub>2</sub> NiO <sub>4</sub>
LiMn <sub>2</sub> O <sub>4</sub> /Li <sub>5</sub> AlO <sub>4</sub>	LiMnO <sub>2</sub> , LiAlO <sub>2</sub> , Li <sub>2</sub> MnO <sub>3</sub>	LiAl <sub>5</sub> O <sub>8</sub> , Li <sub>2</sub> O	$LiAl_5O_8$ , $Li_4Mn_5O_{12}$
LiFePO <sub>4</sub> /Li <sub>5</sub> AlO <sub>4</sub>	FeO, LiAlO <sub>2</sub> , Li <sub>3</sub> PO <sub>4</sub>	LiAlO <sub>2</sub> , LiO <sub>8</sub>	LiAlO <sub>2</sub> , Li <sub>3</sub> PO <sub>4</sub> , Fe <sub>2</sub> O <sub>3</sub>

"The cathode potentials versus bulk Li (in V):  $LiCoO_2$ : 4.2;  $LiNiO_2$ : 4.5;  $LiMnO_2$ : 4.0; NCM532 and NCM811: 4.2;  $LiMn_2O_4$ : 4.0; and  $LiFePO_4$ : 3.50.  $^bNCM532$ :  $Li_6Ni_3Co_2Mn_1O_{12}$ ; NCM811:  $Li_{12}Co_{10}Mn_1Ni_1O_{24}$ .

respectively. Thermodynamically feasible chemical reactions between the electrolyte and various cathodes, namely, layered LiMO<sub>2</sub> (M = Co, Ni, and Mn), spinel LiMn<sub>2</sub>O<sub>4</sub>, and LiFePO4 are detailed in Table 1 and Figures S5–S6 in the Supporting Information. We found that there is no chemical reaction between LAO and layered cathode materials (LXO<sub>2</sub>, X = Co, Ni, and Mn; NCM) listed in the second column in Table 1. However, LAO undergoes a chemical reaction (the second column in Table 1) and an electrochemical reaction (the fourth column in Table 1) at the LiMn<sub>2</sub>O<sub>4</sub>/LAO and LiFePO<sub>4</sub>/Li<sub>5</sub>AlO<sub>4</sub> interfaces and results in the formation of SEI-like (solid-electrolyte interphase, SEI) products. For LAO +  $ne^- \rightarrow C_{\rm equilibrium}$ , LAO will undergo redox decomposition forming SEI-like products with all cathodes at cathodic

potential as listed in the third column in Table 1. The SEI-like composition as the interfacial phase could facilitate the Li passivation in LAO and could be beneficial for cyclability.

To assess the H<sub>2</sub>O and CO<sub>2</sub> stability of LAO, we extend the above method and consider the reactions:  $\alpha \text{LAO} + (1 -$  $(x)H_2O \rightarrow C_{\text{equilibrium}}$  and  $(x)LAO + (1 - x)CO_2 \rightarrow C_{\text{equilibrium}}$ where C<sub>equilibrium</sub> is the low-energy phase equilibrium determined from the phase diagram and x is the mixing parameter varying from 0 and 1. According to the definition (see eqs 4 and 5 in the method), a negative value signifies the thermodynamic feasibility toward  $C_{\text{equilibrium}}$  generation. Table S2 in the Supporting Information shows the chemical reaction equation with maximum reaction energy from the SSE compound and H<sub>2</sub>O/CO<sub>2</sub> molecules into possible products. In the range of 0 and 1 of the mixing parameter, the most favorable reaction of LAO with H<sub>2</sub>O (CO<sub>2</sub>) is 0.4Li<sub>5</sub>GaO<sub>4</sub> +  $0.8H_2O \rightarrow 1.6LiHO + 0.4LiGaO_2 (0.8CO_2 + 0.4Li_5AlO_4 \rightarrow$  $0.8\text{Li}_2\text{CO}_3 + 0.4\text{LiAlO}_2$ ), with a reaction energy of -0.05 eV/atom (-0.22 eV/atom). In Figure 4 and Table S2 in the Supporting Information, we can find that most of the SSE materials (all sulfides, Li<sub>3</sub>Ocl, and LLZO) would react with H<sub>2</sub>O and CO<sub>2</sub> with negative mixing reaction energies, except LTP and LPO. We also note that the extent of H<sub>2</sub>O and CO<sub>2</sub> instability for Li<sub>3</sub>ClO (-0.08 and -0.27 eV/atom) and Li<sub>6</sub>PS<sub>5</sub>Cl (-0.09 and -0.25 eV/atom) is even larger than that for LAO. Moreover, the extent of LAO instability against H<sub>2</sub>O is close to that of LLZO (-0.01 eV/atom). Many experiments have successfully demonstrated the assemblage of Li<sub>3</sub>ClO and Li<sub>6</sub>PS<sub>5</sub>Cl in a battery setup with an argon atmosphere although they are thermodynamically unstable against H<sub>2</sub>O and CO<sub>2</sub>. Thus, thermodynamic H<sub>2</sub>O/CO<sub>2</sub> instability of LAO is less problematic in practice if we can avoid excess exposure to the air.

**3.3. Li-lon Diffusivity in LAO.** For Li-ion diffusivity in LAO, we first evaluate Li-ion diffusion channels of LAO by the bond valence (BV) theory, as shown in Figure 5a,b. For  $\alpha$ -LAO, after careful examination of the bond valence pathway, it is seen that the Li diffusion pathway is constructed piece by piece, by interconnecting the saddle-shaped region (SSR) to form a whole 3D diffusion channel. Our model predicts that

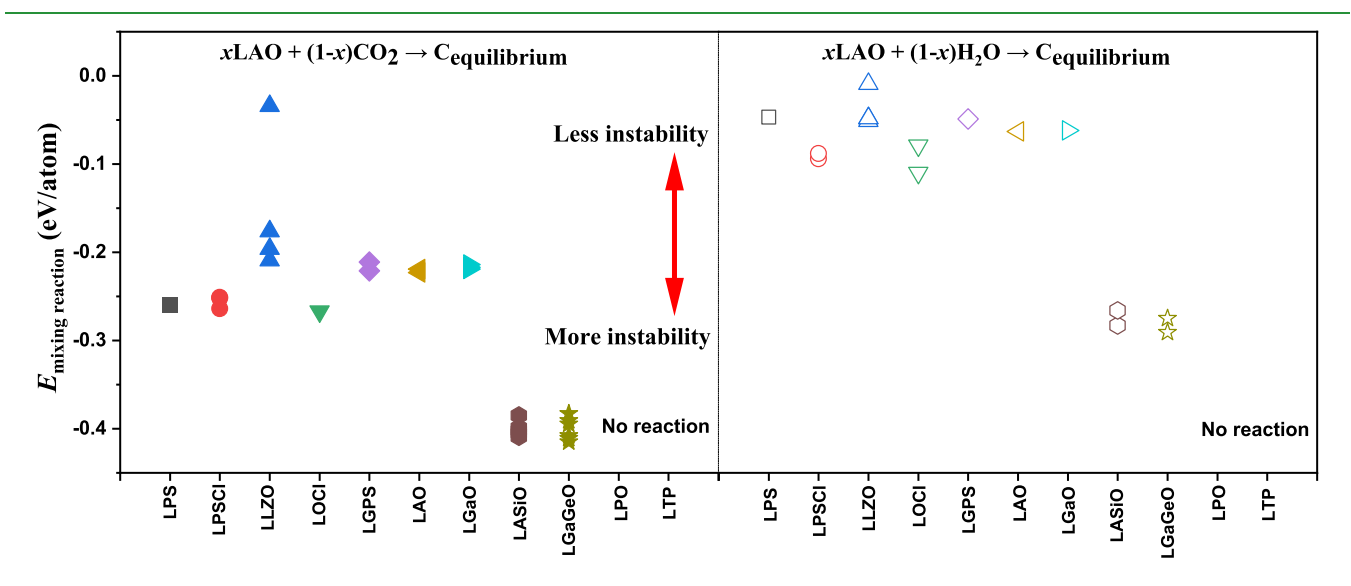


Figure 4. CO<sub>2</sub> stability (left) and moisture stability (right) for LAO, LGO, LAISiO, LGaGeO, and other SSEs (for comparison) are shown. Li<sub>3</sub>PS<sub>4</sub> (LPS), Li<sub>3</sub>OCl (LOCl), Li<sub>3</sub>PO<sub>4</sub> (LPO), and LiTi<sub>2</sub>(PO<sub>4</sub>)<sub>3</sub> (LTP).

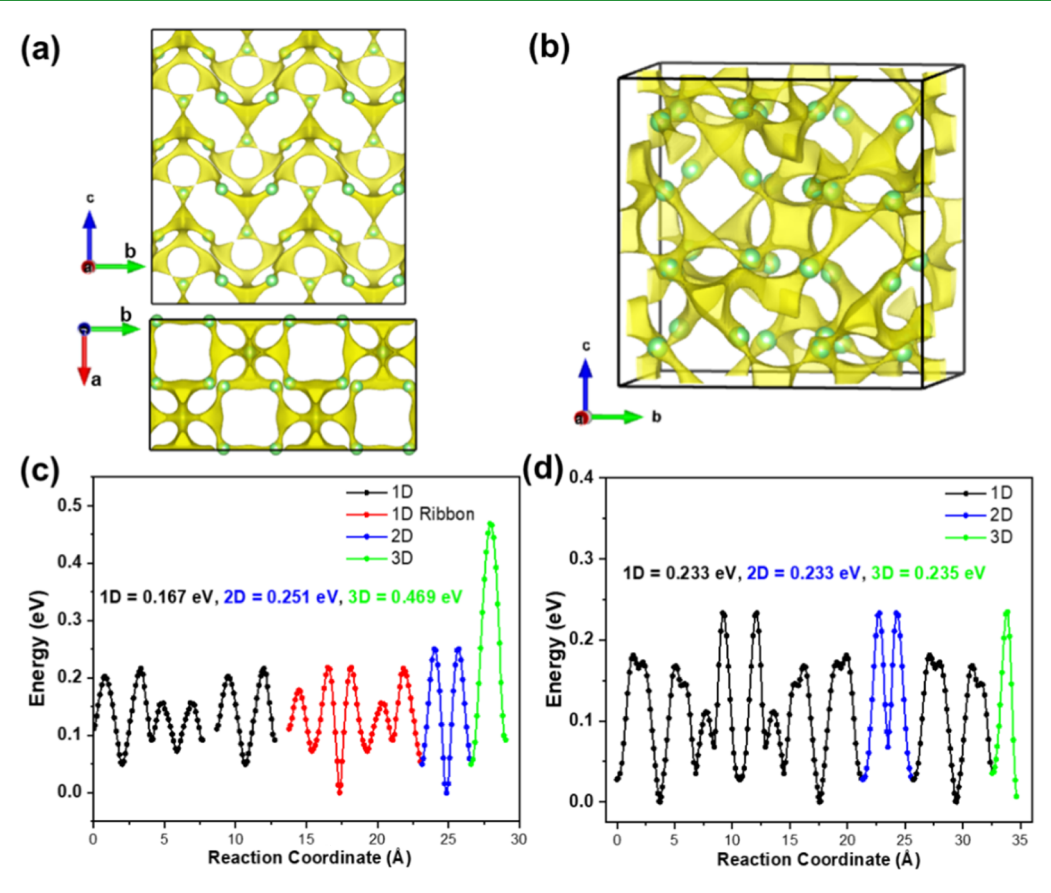
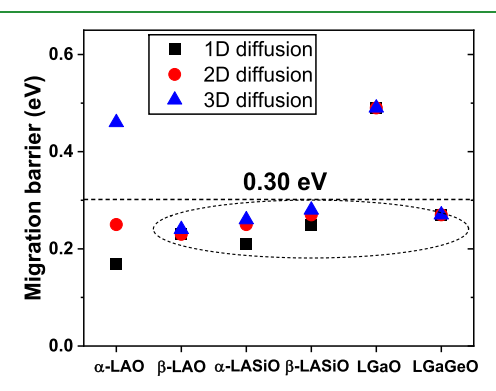


Figure 5. (a,b) Li-ion diffusion channels (obtained from bond valence simulations) in  $\alpha$ - and  $\beta$ -LAO are shown in yellow isosurfaces, respectively. (c,d) BVSE-recommended path and the Li migration barrier in  $\alpha$ - and  $\beta$ -LAO, respectively.

the most favorable interstitial site is just at the saddle-point concerning the Li BV diffusion channel (i.e., I1 and I3 sites shown in the following Figure 7a). For  $\beta$ -LAO in Figure 5b (BV analysis), there is a 3D diffusion channel. The BVSE results (Figure 5c,d) show the 1D, 2D, and 3D migration barriers in  $\alpha$ - and  $\beta$ -LAO. It can be seen that the 1D migration barriers in  $\alpha$ -LAO and 3D migration barriers in  $\beta$ -LAO are sufficiently low that the Li-ions can diffuse within them. For example, the 1D migration barrier is 0.17 eV in  $\alpha$ -LAO, which is even less than that for LGPS (0.20  $\pm$  0.02 eV). Such a low energy potential surface in LAO also suggests that there may be plenty of Li interstitial sites (or metastable sites) along the Li diffusion path. To prove the diffusion pattern, the AIMD simulations at 850 K are performed within  $\alpha$ - and  $\beta$ -LAO (Figure S7 in the Supporting Information). The mean square displacement (MSD) results of Li-ions are consistent with the suggestion of BVSE. There is definitely anisotropic diffusion in  $\alpha$ -LAO and a nearly isotropic 3D diffusion in  $\beta$ -LAO.  $\alpha$ -LAO exhibits negligible diffusion along the a-axis direction but a significant diffusion along the c-axis direction. Therefore, we suggest that there is an anisotropic and a nearly isotropic diffusion in pure  $\alpha$ - and  $\beta$ -LAO, respectively.

The above diffusion calculations suggest that the layout of AlO<sub>4</sub> and LiO<sub>4</sub> units causes the anisotropic ion transport in  $\alpha$ -LAO. Previous studies suggested that the formation of solid solutions can significantly improve the ionic conductivity and tune Li diffusion paths, such as in the range of compounds Li<sub>4</sub>SiO<sub>4</sub>, Li<sub>4-x</sub>Si<sub>1-x</sub>P<sub>x</sub>O<sub>4</sub>, Li<sub>4+x</sub>Si<sub>1-x</sub>Al<sub>x</sub>O<sub>4</sub>, or Li<sub>4</sub>Al<sub>x</sub>Si<sub>1-2x</sub>P<sub>x</sub>O<sub>4</sub>. Therefore, the motif-based design of a polyanion mixing class of (Si/Al)O<sub>4</sub> and (Ga/Ge)O<sub>4</sub> units

may modify the potential energy surface and lower the migration barriers. It is well known that a 3D diffusion pattern is more robust than a 1D diffusion one. To further lower the migration barrier of Li, we calculate the migration barrier along with three directions in  $\alpha$ -LASiO,  $\beta$ -LASiO, LGaO, and LgaGeO, as shown in Figure 6 (the original copy of Figure 5 is



**Figure 6.** Li migration barrier obtained from BVSE in  $\alpha$ - and  $\beta$ -LAO,  $\alpha$ -LASiO,  $\beta$ -LASiO, LGaO, and LGaGeO. The short-dashed circle suggests the compounds with low migration barriers.

listed in Figures S8–S13 in the Supporting Information). We note that Si-substitution of Al in  $\alpha$ -LASiO and Ge-substitution of Ga in LGaGeO can significantly decrease the Li migration barrier of their parent structures, which is consistent with an effect called the "mixed polyanion" effect. The mixed polyanion effect also causes the substituted composition of

 $\alpha$ -LASiO to show a 2D-3D transition in the Li diffusion pattern.

To evaluate the correlation between the chemical composition and the structure evolution, several intrinsic structural and energy characteristics of  $XO_4$  tetrahedra ( $X = AI^{3+}$ ,  $Ga^{3+}$ ,  $Si^{4+}$ , and  $Ge^{4+}$ ) are listed in Table 2. Based on the

Table 2. Tetrahedral Anion Charge  $((XO_4)^{n-})$ , the X-O Distance in the  $XO_4$  unit of  $\text{Li}_z XO_4$   $(d_{(X-O)})$ , X-O Dissociation Energy in the  $XO_4$  unit  $(\text{Ed}_{(X-O)})$ , the Li-X Distance in the Li-XO<sub>4</sub> configuration  $(d_{(X-O)})$ , and the Binding Energy between Li and the  $(XO_4)$  Unit  $(\text{Eb}_{(\text{Li}-XO_4)})$ 

$(XO_4)^{n-}$	$d_{(X-O)}(A)$	$Ed_{(X-O)}$ (eV)	$d_{(\text{Li-X})}$ (Å)	$Eb_{(Li-XO_4)}(eV) \\$
$(AlO_4)^{5-}$	1.78	2.21	2.49	-5.28
$(SiO_4)^{4-}$	1.64	3.21	2.43	-5.91
$(GaO_4)^{5-}$	1.83	1.80	2.43	-5.22
$(GeO_4)^{4-}$	1.77	2.36	2.47	-5.46

results of the X-O distance, X-O dissociation energy, and Li-X distance in the Li-XO<sub>4</sub> configuration, the substitution of (Al/Ga)<sup>3+</sup> with (Si/Ge)<sup>4+</sup> within the XO<sub>4</sub> tetrahedrons makes the X-O bonds have a shorter and stronger bonding interaction. This variation in the bonding interaction and the volume of XO<sub>4</sub> tetrahedrons is reflected in the distortion of  $\text{LiO}_{v}$  polyhedra in  $\text{Li}_{5-x}M_{1-x}M'_{x}O_{4}$ . The binding energy between Li and (XO<sub>4</sub>) units shows a difference of 0.63 eV between Li-AlO<sub>4</sub> and Li-SiO<sub>4</sub> and 0.24 eV between Li-GaO<sub>4</sub> and Li-GeO<sub>4</sub>. The non-uniform bonding interaction for different Li-XO<sub>4</sub> may modify the overall potential energy surface. Therefore, in LAO and LGaO, Li-ions occupy a much more uniform potential energy surface and LiO, polyhedra, and the energy barrier is relatively high. In the substituted LASO and LGaGeO compounds, the mixing of these XO<sub>4</sub> groups with varied LiO, polyhedra and bonding interaction of Eb<sub>(Li-XO<sub>4</sub>)</sub> may result in lower barriers and transition of the Limigration pattern.

To further identify the migration barriers of Li-ions in  $\alpha$ - and  $\beta$ -LAO, we then calculate the Li migration process through the Cl-NEB method. The ionic conductivity of LAO stems from the diffusion of point defects, including the Li vacancy and Li interstitial.<sup>22</sup> For  $\alpha$ -LAO (Figure 7a), we evaluate a 3D diffusion path, including intra- and inter-SSR, as shown in the insets of Figure 7a. Along the Li vacancy path, the migrating Li will pass through Li1, Li2, and Li3, and the vacancy migration barrier is calculated to be as high as 0.75 eV in the Li2  $\rightarrow$  Li3 path. Along the Li interstitial path, the migrating Li interstitial will pass I1, I2, Li4, and I3, where the Li interstitial site (I1 or I2) migrates to the lattice site (Li4), meanwhile lattice Li migrates to the interstitial site (I3). Li interstitial migration barriers in the paths: I1  $\rightarrow$  I2 and Li4  $\rightarrow$  I3 are 0.30 and 0.38 eV, respectively, which are substantially lower than that of Li vacancy diffusion. For  $\beta$ -LAO (Figure 7b), we also check one 3D diffusion path, where Li1' and Li2' are at the same diffusion channel (i.e., along the a-axis direction) but Li3' is at the adjacent diffusion channel. We find that the Li vacancy migration barrier in the path:  $Li1' \rightarrow Li2'$  (0.35 eV) is much lower than that in the path:  $Li2' \rightarrow Li3'$  (0.63 eV) and Li interstitial migration barrier in the path: Li1'  $\rightarrow$  I1'  $\rightarrow$  Li2' (0.34 eV) is also lower than that in the path:  $I2' \rightarrow Li3' \rightarrow I3'$ (0.40 eV), suggesting a-axis direction diffusion is more favorable. The different migration barriers further demonstrate that Li diffusion in LAO is highly anisotropic; for example, in  $\beta$ -LAO, it is easier along the a-axis direction but harder along the b-axis direction. Therefore, based on the Cl-NEB calculations, we conclude that the overall 3D migration barrier in  $\alpha$ -LAO is about 0.38 eV, and from eqs 2 and 3, the diffusion coefficient and ionic conductivity at room temperature (300 K) are  $2.83 \times 10^{-9}$  cm<sup>2</sup> s<sup>-1</sup> and  $9.12 \times 10^{-4}$  S cm<sup>-1</sup>, respectively. The overall 3D migration barrier in  $\beta$ -LAO is about 0.40 eV and the diffusion coefficient and ionic conductivity at room temperature are  $1.31 \times 10^{-9} \text{ cm}^2 \text{ s}^{-1}$ and  $4.28 \times 10^{-4}$  S cm<sup>-1</sup>, respectively. The ionic conductivity of Li ions in LAO has a magnitude equal to that of the LLZO,<sup>38</sup>

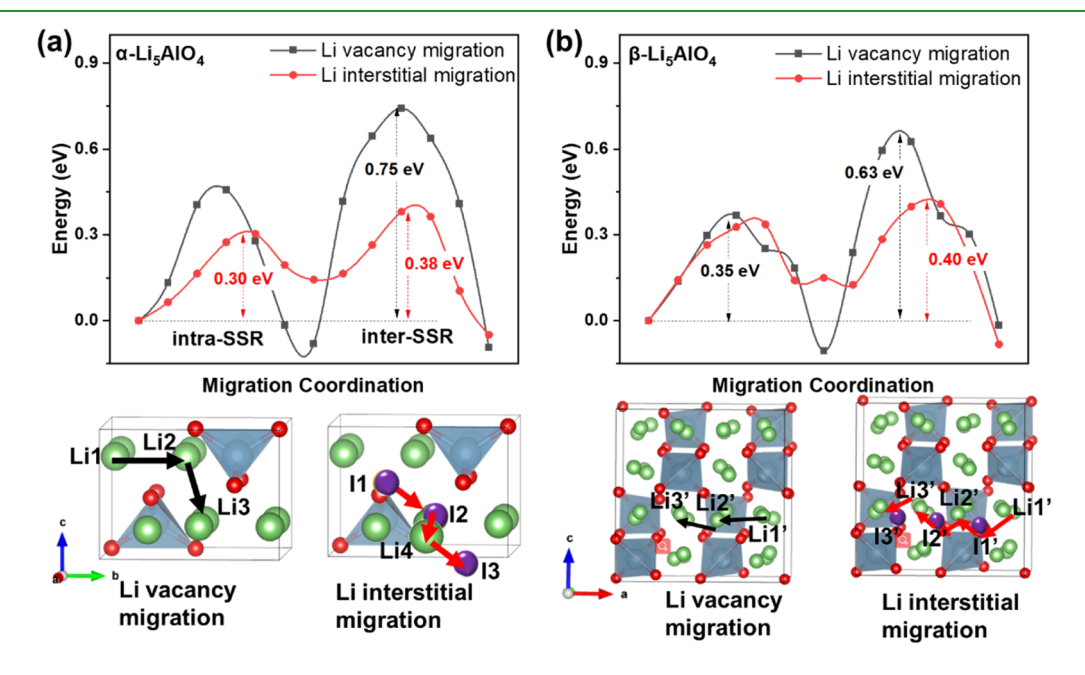


Figure 7. (a,b) Energy profiles and configurations of Li direct hopping via vacancy and Li interstitial migration via interstitial sites, respectively. The tetrahedrons represent the  $AlO_4$  units.

implying a good performance of the battery when using LAO SSE. Overall, the interstitial migration in LAO is more favorable for Li diffusion. This may be rationalized by the brief appearance of Li vacancies and the stable coordination environment maintained during the Li interstitial migration. Therefore, the introduction of lithium interstitial defects is crucial to high conductivity, and fortunately that a large Liinterstitial defect concentration is possible in Li<sub>5+x</sub>Al<sub>1-x</sub>Zn<sub>x</sub>O<sub>4</sub>, potentially allowing it to exceed the conductivity of LAO. Therefore, we can anticipate that LAO-based family SSE materials, with their high ionic conductivity and electrochemical stability, will profoundly improve the overall electrochemical performance of solid-state batteries.

#### 4. CONCLUSIONS

In summary, we have applied the first-principles-based DFT methods to explore the phase structure, defect chemistry, electrochemical properties, and Li-ion conduction of  $\alpha$ - and  $\beta$ -LAO to overcome the key challenge of combining stability with high Li-ion conductivity. We have identified LAO as an oxide class of SSE for ASSLBs. The electrochemical stability window of LAO is found to be [0.01-3.20 V] versus Li<sup>+</sup>/Li. The LAO forms a stable interface with relatively high-voltage LCoO<sub>2</sub> and forms SEI-like interfacial phases with LiNiO<sub>2</sub>, LiMnO<sub>2</sub>, LiMn<sub>2</sub>O<sub>4</sub>, and LiFePO<sub>4</sub> cathodes. The Li interstitial migration has a migration barrier in  $\alpha$ -LAO as low as 0.38 eV. In  $\beta$ -LAO, there are migration barriers of 0.34 eV for 1D diffusion and 0.40 eV for 3D diffusion. Si (or Ge) substitution at Al (or Ga) sites improves its Li-ion mobility but reduces the electrochemical stability window slightly. The calculated Li-ion diffusion coefficients (Li-ion conductivities) for  $\alpha$ - and  $\beta$ -LAO at room temperature are about  $2.83 \times 10^{-9}$  cm<sup>2</sup> s<sup>-1</sup> (9.12 ×  $10^{-4} \text{ S cm}^{-1}$  and  $1.31 \times 10^{-9} \text{ cm}^2 \text{ s}^{-1} (4.28 \times 10^{-4} \text{ S cm}^{-1})$ , respectively. Indeed, an important reason for this good conductivity is the arrangement of (Li/Al)O<sub>4</sub> units in  $\alpha$ - and  $\beta$ -LAO structures, which allows considerable energy minimum sites for Li-ions and a percolating network of Li-ion diffusion. Overall, LAO is a potential candidate for SSE materials that can balance the stability and ionic conductivity and therefore deserves further experimental examination.

# ASSOCIATED CONTENT

# Supporting Information

The Supporting Information is available free of charge at https://pubs.acs.org/doi/10.1021/acsami.1c19922.

> Structural parameters and crystal structure of  $\alpha$ - and  $\beta$ -LAO; TDOS of LAO and LGaO; voltage profile and phase equilibria of LASiO, LGaO, and LGaGeO; mixing reactions with cathodes and SSE materials; mixing reaction between SSE materials and H2O or CO2; and original Li-ion diffusion path as recommended by BVSE (PDF)

#### AUTHOR INFORMATION

# **Corresponding Authors**

Bingkai Zhang - Guangzhou Key Laboratory of Clean Transportation Energy Chemistry, School of Chemical Engineering and Light Industry, Guangdong University of Technology, Guangzhou 510006, China; Email: zhangbk@ gdut.edu.cn

Feng Pan - School of Advanced Materials, Peking University Shenzhen Graduate School, Shenzhen 518055, China;

orcid.org/0000-0002-8216-1339; Email: panfeng@ pku.edu.cn

Zhan Lin - Guangzhou Key Laboratory of Clean Transportation Energy Chemistry, School of Chemical Engineering and Light Industry, Guangdong University of Technology, Guangzhou 510006, China; o orcid.org/0000-0001-5009-8198; Email: zhanlin@gdut.edu.cn

#### Author

Jiajie Zhong - Guangzhou Key Laboratory of Clean Transportation Energy Chemistry, School of Chemical Engineering and Light Industry, Guangdong University of Technology, Guangzhou 510006, China

Complete contact information is available at: https://pubs.acs.org/10.1021/acsami.1c19922

#### **Notes**

The authors declare no competing financial interest.

#### ACKNOWLEDGMENTS

This work was supported by GuangDong Basic and Applied Basic Research Foundation (2020A1515110046).

#### REFERENCES

- (1) Lin, Z.; Liu, T.; Ai, X.; Liang, C. Aligning Academia and Industry for Unified Battery Performance Metrics. Nat. Commun. 2018, 9,
- (2) Zhang, B.; Tan, R.; Yang, L.; Zheng, J.; Zhang, K.; Mo, S.; Lin, Z.; Pan, F. Mechanisms and Properties of Ion-Transport in Inorganic Solid Electrolytes. Energy Storage Mater. 2018, 10, 139-159.
- (3) Minafra, N.; Hogrefe, K.; Barbon, F.; Helm, B.; Li, C.; Wilkening, H. M. R.; Zeier, W. G. Two-Dimensional Substitution: Toward a Better Understanding of the Structure-Transport Correlations in the Li-Superionic Thio-LISICONs. Chem. Mater. **2021**, 33, 727-740.
- (4) Wang, C.; Liang, J.; Zhao, Y.; Zheng, M.; Li, X.; Sun, X. All-Solid-State Lithium Batteries Enabled by Sulfide Electrolytes: From Fundamental Research to Practical Engineering Design. Energy Environ. Sci. 2021, 14, 2577-2619.
- (5) Rajagopalan, R.; Zhang, Z.; Tang, Y.; Jia, C.; Ji, X.; Wang, H. Understanding Crystal Structures, Ion Diffusion Mechanisms and Sodium Storage Behaviors of NASICON Materials. Energy Storage Mater. 2021, 34, 171-193.
- (6) Li, Y.; Han, J. T.; Wang, C. A.; Xie, H.; Goodenough, J. B. Optimizing Li<sup>+</sup> Conductivity in a Garnet Framework. J. Mater. Chem. 2012, 22, 15357-15361.
- (7) Wang, C.; Fu, K.; Kammampata, S. P.; McOwen, D. W.; Samson, A. J.; Zhang, L.; Hitz, G. T.; Nolan, A. M.; Wachsman, E. D.; Mo, Y.; Thangadurai, V.; Hu, L. Garnet-Type Solid-State Electrolytes: Materials, Interfaces, and Batteries. Chem. Rev. 2020, 120, 4257-4300.
- (8) Zhao, Y.; Daemen, L. L. Superionic Conductivity in Lithium-Rich Anti-Perovskites. J. Am. Chem. Soc. 2012, 134, 15042-15047.
- (9) Dawson, J. A.; Attari, T. S.; Chen, H.; Emge, S. P.; Johnston, K. E.; Islam, M. S. Elucidating Lithium-ion and Proton Dynamics in Anti-Perovskite Solid Electrolytes. Energy Environ. Sci. 2018, 11, 2993-3002.
- (10) Li, X.; Liu, J.; Banis, M. N.; Lushington, A.; Li, R.; Cai, M.; Sun, X. Atomic Layer Deposition of Solid-State Electrolyte Coated Cathode Materials with Superior High-Voltage Cycling Behavior for Lithium Ion Battery Application. Energy Environ. Sci. 2014, 7, 768-
- (11) Ding, X.; Luo, D.; Cui, J.; Xie, H.; Ren, Q.; Lin, Z. An Ultra-Long-Life Lithium-Rich Li<sub>1,2</sub>Mn<sub>0,6</sub>Ni<sub>0,2</sub>O<sub>2</sub> Cathode by Three-in-One Surface Modification for Lithium-Ion Batteries. Angew. Chem., Int. Ed. **2020**, *59*, 7778–7782.

- (12) Famprikis, T.; Canepa, P.; Dawson, J. A.; Islam, M. S.; Masquelier, C. Fundamentals of Inorganic Solid-State Electrolytes for Batteries. *Nat. Mater.* **2019**, *18*, 1278–1291.
- (13) Maiti, S.; Sclar, H.; Sharma, R.; Vishkin, N.; Fayena-Greenstein, M.; Grinblat, J.; Talianker, M.; Burstein, L.; Solomatin, N.; Tiurin, O.; Ein-Eli, Y.; Noked, M.; Markovsky, B.; Aurbach, D. Understanding the Role of Alumina (Al<sub>2</sub>O<sub>3</sub>), Pentalithium Aluminate (Li<sub>5</sub>AlO<sub>4</sub>), and Pentasodium Aluminate (Na<sub>5</sub>AlO<sub>4</sub>) Coatings on the Li and Mn-Rich NCM Cathode Material 0.33Li<sub>2</sub>MnO<sub>3</sub>·0.67Li(Ni<sub>0.4</sub>Co<sub>0.2</sub>Mn<sub>0.4</sub>)O<sub>2</sub> for Enhanced Electrochemical Performance. *Adv. Funct. Mater.* **2021**, *31*, 2008083
- (14) Zhou, J.; Wang, Q.; Zhang, M.; Guo, Y.; Zhu, A.; Qiu, X.; Wu, H.; Chen, X.; Zhang, Y. In Situ Formed Li<sub>5</sub>AlO<sub>4</sub>-Coated LiNi<sub>0.8</sub>Co<sub>0.1</sub>Mn<sub>0.1</sub>O<sub>2</sub> Cathode Material Assisted by Hydrocarbonate with Improved Electrochemical Performance for Lithium-Ion Batteries. *Electrochim. Acta* **2020**, 353, 136541.
- (15) Sharma, A.; Chourasia, N. K.; Sugathan, A.; Kumar, Y.; Jit, S.; Liu, S.-W.; Pandey, A.; Biring, S.; Pal, B. N. Solution Processed Li<sub>5</sub>AlO<sub>4</sub> Dielectric for Low Voltage Transistor Fabrication and Its Application in Metal Oxide/Quantum Dot Heterojunction Phototransistors. *J. Mater. Chem. C* **2018**, *6*, 790–798.
- (16) Ávalos-Rendón, T. L.; Pfeiffer, H. High CO<sub>2</sub> Chemisorption in A-Li<sub>s</sub>AlO<sub>4</sub> at Low Temperatures (30-80 °C): Effect of the Water Vapor Addition. *Energy Fuels* **2012**, *26*, 3110–3114.
- (17) Johnson, R. T.; Biefeld, R. M. Ionic Conductivity of Li<sub>5</sub>AlO<sub>4</sub> and Li<sub>5</sub>GaO<sub>4</sub> in Moist Air Environments: Potential Humidity Sensors. *Mater. Res. Bull.* **1979**, *14*, 537–542.
- (18) Johnson, R. T.; Biefeld, R. M.; Keck, J. D. Ionic Conductivity in Li<sub>c</sub>AlO<sub>4</sub> and Lioh. *Mater. Res. Bull.* **1977**, *12*, 577–587.
- (19) Xiao, R.; Li, H.; Chen, L. Candidate Structures for Inorganic Lithium Solid-State Electrolytes Identified by High-Throughput Bond-Valence Calculations. *J. Materiomics* **2015**, *1*, 325–332.
- (20) Islam, M. S.; Fisher, C. A. J. Lithium and Sodium Battery Cathode Materials: Computational Insights into Voltage, Diffusion and Nanostructural Properties. *Chem. Soc. Rev.* **2014**, *43*, 185–204.
- (21) Kresse, G.; Furthmüller, J. Efficient Iterative Schemes for Ab Initio Total-Energy Calculations Using a Plane-Wave Basis Set. *Phys. Rev. B: Condens. Matter Mater. Phys.* **1996**, *54*, 11169–11186.
- (22) Perdew, J. P.; Chevary, J. A.; Vosko, S. H.; Jackson, K. A.; Pederson, M. R.; Singh, D. J.; Fiolhais, C. Atoms, Molecules, Solids, and Surfaces: Applications of the Generalized Gradient Approximation for Exchange and Correlation. *Phys. Rev. B: Condens. Matter Mater. Phys.* 1992, 46, 6671–6687.
- (23) Kresse, G.; Furthmüller, J. Efficiency of Ab-Initio Total Energy Calculations for Metals and Semiconductors Using a Plane-Wave Basis Set. *Comput. Mater. Sci.* 1996, 6, 15–50.
- (24) Blöchl, P. E. Projector Augmented-Wave Method. Phys. Rev. B: Condens. Matter Mater. Phys. 1994, 50, 17953-17979.
- (25) Chen, H.; Wong, L. L.; Adams, S. Softbv-a Software Tool for Screening the Materials Genome of Inorganic Fast Ion Conductors. *Acta Crystallogr., Sect. B: Struct. Sci., Cryst. Eng. Mater.* **2019**, 75, 18–33.
- (26) Wong, L. L.; Phuah, K. C.; Dai, R.; Chen, H.; Chew, W. S.; Adams, S. Bond Valence Pathway Analyzer-an Automatic Rapid Screening Tool for Fast Ion Conductors within Softby. *Chem. Mater.* **2021**, *33*, 625–641.
- (27) Henkelman, G.; Uberuaga, B. P.; Jónsson, H. A Climbing Image Nudged Elastic Band Method for Finding Saddle Points and Minimum Energy Paths. *J. Chem. Phys.* **2000**, *113*, 9901–9904.
- (28) Henkelman, G.; Jónsson, H. Improved Tangent Estimate in the Nudged Elastic Band Method for Finding Minimum Energy Paths and Saddle Points. *J. Chem. Phys.* **2000**, *113*, 9978–9985.
- (29) Kirklin, S.; Meredig, B.; Wolverton, C. High-Throughput Computational Screening of New Li-Ion Battery Anode Materials. *Adv. Energy Mater.* **2013**, 3, 252–262.
- (30) Wolverton, C.; Siegel, D. J.; Akbarzadeh, A. R.; Ozoliņš, V. Discovery of Novel Hydrogen Storage Materials: An Atomic Scale Computational Approach. *J. Phys.: Condens. Matter* **2008**, *20*, 064228.

- (31) Richards, W. D.; Miara, L. J.; Wang, Y.; Kim, J. C.; Ceder, G. Interface Stability in Solid-State Batteries. *Chem. Mater.* **2016**, 28, 266–273.
- (32) Ong, S. P.; Wang, L.; Kang, B.; Ceder, G. Li-Fe-P-O<sub>2</sub> Phase Diagram from First Principles Calculations. *Chem. Mater.* **2008**, *20*, 1798–1807.
- (33) Ong, S. P.; Mo, Y.; Richards, W. D.; Miara, L.; Lee, H. S.; Ceder, G. Phase Stability, Electrochemical Stability and Ionic Conductivity of the  $\text{Li}_{10+/-1}\text{MP}_2\text{X}_{12}$  (M = Ge, Si, Sn, Al or P, and X = O, S or Se) Family of Superionic Conductors. *Energy Environ. Sci.* **2013**, *6*, 148–156.
- (34) Ong, S. P.; Richards, W. D.; Jain, A.; Hautier, G.; Kocher, M.; Cholia, S.; Gunter, D.; Chevrier, V. L.; Persson, K. A.; Ceder, G. Python Materials Genomics (Pymatgen): A Robust, Open-Source Python Library for Materials Analysis. *Comput. Mater. Sci.* **2013**, *68*, 314–319.
- (35) Banerjee, S.; Zhang, X.; Wang, L.-W. Motif-Based Design of an Oxysulfide Class of Lithium Superionic Conductors: Toward Improved Stability and Record-High Li-Ion Conductivity. *Chem. Mater.* **2019**, *31*, 7265–7276.
- (36) Deng, Y.; Eames, C.; Fleutot, B.; David, R.; Chotard, J.-N.; Suard, E.; Masquelier, C.; Islam, M. S. Enhancing the Lithium Ion Conductivity in Lithium Superionic Conductor (LISICON) Solid Electrolytes through a Mixed Polyanion Effect. *ACS Appl. Mater. Interfaces* **2017**, *9*, 7050–7058.
- (37) Deng, Y.; Eames, C.; Chotard, J.-N.; Lalère, F.; Seznec, V.; Emge, S.; Pecher, O.; Grey, C. P.; Masquelier, C.; Islam, M. S. Structural and Mechanistic Insights into Fast Lithium-Ion Conduction in Li<sub>4</sub>SiO<sub>4</sub>-Li<sub>3</sub>PO<sub>4</sub> Solid Electrolytes. *J. Am. Chem. Soc.* **2015**, 137, 9136–9145.
- (38) Shao, C.; Liu, H.; Yu, Z.; Zheng, Z.; Sun, N.; Diao, C. Structure and Ionic Conductivity of Cubic Li<sub>7</sub>La<sub>3</sub>Zr<sub>2</sub>O<sub>12</sub> Solid Electrolyte Prepared by Chemical Co-Precipitation Method. *Solid State Ionics* **2016**, 287, 13–16.